# Fully Integrated Electronic-Photonic Ultrasound Receiver Array for Endoscopic Applications in a Zero-Change 45nm CMOS-SOI Process

Panagiotis Zarkos, *Member, IEEE*, Sidney Buchbinder, *Student Member, IEEE*, Christos Adamopoulos, *Member, IEEE*, Sarika Madhvapathy, *Student Member, IEEE*, Olivia Hsu, *Student Member, IEEE*, Jake Whinnery, Pavan Barghava, *Member, IEEE*, and Vladimir Stojanović, *Senior Member, IEEE* 

Abstract—This paper presents the first fully integrated 2-D array of electronic-photonic ultrasound sensors targeting lowpower miniaturized ultrasound probes for endoscopic applications. Fabricated in a zero-change 45nm CMOS-SOI technology this  $5.53 \times 3.03$  mm<sup>2</sup> Electronic-Photonic System on Chip (EPSoC), utilizes micro-ring resonators (MRRs) as ultrasound sensors instead of the traditional piezoelectric or capacitive micromachined transducers (PMUTs or CMUTs). The photonic nature of the sensor enables remoting of the power-hungry receive electronics outside the probe tip, thus lowering the power dissipation inside the human body. Moreover, it eliminates electrical cabling replacing the bulky micro-coax cables with thinner optic fibers. This EPSoC also reduces fiber count by 8x with zero power and area overhead by performing wavelength division multiplexed (WDM) interrogation of MRR sensors coupled onto the same waveguide in-lieu of sub-array beamforming or in-pixel digitization. Leveraging the monolithic integration of photonic devices with CMOS circuitry, a complete receiver unit is built right next to the sensor MRRs, including a programmable gain transimpedance amplifier (TIA) and background current cancellation digital-to-analog converters IDACS, which allow for a sensor operating range of 74dB. A 9-bit SAR ADC performs on-chip A/D conversion making for a self-contained endoscopic ultrasound receiver system. The photonic sensing element demonstrates 7.3 mV/kPa sensitivity, while consuming 0.43 mW of power and 0.01 mm<sup>2</sup> of area. The functionality of the fabricated chip has been demonstrated in ultrasonic receiver beamforming experiments.

Index Terms—3-D ultrasound imaging, microring resonator (MRR), wavelength division multiplexing (WDM), optical ultrasound, silicon photonics, monolithic integration, ultrasound sensors, system on chip (SoC), real-time, point-of-care.

# I. INTRODUCTION

LTRASOUND imaging has long been an indispensable tool in numerous fields of diagnostic and interventional medicine. Low-cost and minimally invasive ultrasound imaging systems have been reliably providing images of various body parts for several decades. However, endoscopes targeting

Manuscript received May 8, 2022. (Corresponding author: Panagiotis Zarkos)

P. Zarkos, S. Buchbinder, C. Adamopoulos, S. Madhvapathy, P. Bhargava, and V. Stojanović are with the Department of Electrical Engineering and Computer Science, University of California, Berkeley, CA 94720 USA (e-mail: panzarkos@berkeley.edu)

O. Hsu was with the Department of Electrical Engineering and Computer Science, University of California, Berkeley, CA 94720 USA. She is now with the Department of Electrical Engineering, Stanford University, Stanford, CA 94305 USA.

J. Whinnery is with the Department of Mechanical Engineering, University of California, Berkeley, CA 94720 USA

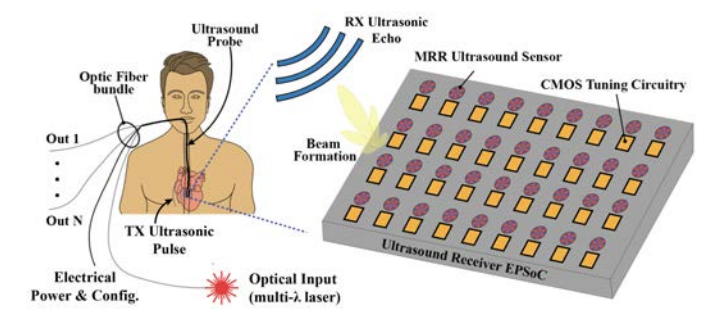


Fig. 1. Endoscopic ultrasound paradigm emphasizing the RX path: A TEE probe using electrically tuned MRR ultrasound sensors to perform RX beamforming. Optic fiber I/O, electrical power and configuration signals, and TX/RX ultrasound pulse echo are also illustrated.

intravascular and catheterized applications there face an unmet need for real-time, high-resolution 3-D ultrasonic images that would greatly enhance the physician's comprehension of the patient's physiology in both interventional and diagnostic settings. Intravascular ultrasound (IVUS)-guided stent placement [1], and transesophageal echocardiography (TEE) [2], [3], constitute characteristic paradigms in which 3-D endoscopic ultrasound imaging can aid during both the time of surgery and the first steps of diagnosis or therapy of cardiovascular diseases.

In order to acquire high resolution volumetric images, nextgeneration ultrasound imaging systems need to integrate thousands of sensing elements in dense 2-D arrays of piezoelectric or capacitive micromachined ultrasound transducers (PMUTs and CMUTs) inside the device's probe-head. The size of these next-generation endoscopic probes is limited by safety regulations to  $1 \text{cm}^3$  for the probe-head and 5 - 7 mm for the probe tube diameter [4]. To ensure optimal lateral resolution and SNR is achieved on the RX beamforming path, the entire available receiver aperture should be arrayed with sensors. At the same time, to avoid formation of grating lobes the sensor pitch should be limited to  $< \lambda/2$  [5]. Combining these conditions translates to arrays with  $\sim 1000$  elements, which are practically impossible to fan-out electrically using microcoax cables while complying with the aforementioned probe diameter limit.

Hence, the vast majority of the proposed solutions in literature perform local channel reduction using dedicated front-end circuitry, 3-D integrated directly underneath the transducer array in the probe head. The most popular ones

either employ sub-array beamforming or direct element digitization to achieve this channel reduction [6]–[8], architectural approaches which both place two stringent requirements on the application specific integrated circuit (ASIC) design: (a) the size of each pixel-matched receiver unit needs to be below  $\lambda/2$  to ensure the array FOV is maximized and no compromises on the image are made, and (b) to avoid probe heat-up, a safety regulation limit of 0.5W needs to be upheld [9], amounting to < 0.5mW per receiver for 1000 element arrays. Time-division multiplexing [10], [11], and switching schemes [12], [13] have also been proposed to allow multiple elements to share a single cable. Both of these approaches tend to reduce channel count at the expense of additional hardware, thus driving up area and power dissipation, an aspect that is not particularly desirable in modern PoC application settings such as [14].

In an attempt to tackle the above challenges, alternative solutions based on optical sensors have recently been reported. Implementations using optical transducers can eliminate the electrical cabling, replacing micro-coax cables with much thinner optic fibers. Interferometric and refractometric devices with very high sensitivity, based on Fabry-Perot cavities [15], [16], fiber Bragg gratings [17], [18], and polarization dependent reflection [19] have been proposed. However, these devices are either not easy to array due to relatively large footprints or require complicated scanning configurations precluding them from use in POC-type systems. On the contrary, optical micro-ring resonator (MRR) sensors are an ideal candidate for such applications, since they have compact footprints (down to 10μm), and competitive sensitivity [20]–[22]. One major drawback of the MRR based ultrasound receiver arrays presented to date is the lack of a robust on-chip resonance tuning mechanism [23], [24]. Given that MRR based sensors rely on matching the wavelength of the incoming laser to the stable side of the Lorentzian shaped resonant spectrum, the inability to reliably tune the MRR resonance necessitates the use of expensive, bulky tunable lasers, instead of lowcost fixed-wavelength light sources, and prohibits real-time simultaneous interrogation of all the sensor elements in the array.

In this work, we present a first-of-its-kind Electronic-Photonic System-on-Chip (EPSoC) that achieves real-time simultaneous interrogation of multiple MRR sensors arrayed in a 2-D matrix, as an extension of our work in [25]. This is primarily enabled by utilizing a fully integrated electronicphotonic biosensing platform in a high volume advanced CMOS-SOI process. Our proof-of-concept EPSoC prototype is fabricated in the GlobalFoundries 45nm SOI CMOS technology node, which allows monolithic integration of photonic devices (waveguides and planar MRRs) with high-performance CMOS circuits on the same chip. This tight co-integration of photonics and electronics results in efficient and robust thermal control of the MRR resonant wavelength. To fully exploit this unique capability we introduce a dual-chip sensing receiver architecture, which enables ultra-low power and area operation, while maintaining a very low overall system form-factor, compatible with the specifications of modern endoscopes outlined above. This first EPSoC prototype can flexibly be configured as a sensing or as a receiver chip and it supports an  $8\times4$  sensor

array, with each sensing unit including a variable gain signal conditioning stage, followed by a successive approximation register (SAR) analog-to-digital converter (ADC), while on-chip serialization and current mode logic (CML) output driver stages have also been implemented. An endoscopic ultrasound sensing device based on the proposed EPSoC is illustrated in Fig. 1.

Since the MRR based receivers lack transmit functionality the focus is placed on the ultrasound receive path in this paper. However, a small dedicated piezoelectric transmitter array could be co-packaged with this EPSoC reveiver array to implement TX functionality, similarly to what was proposed in [26]. Implementations of multi-modal TX-RX optical ultrasound have also been reported in literature [27], where a dichroic filter is used to generate ultrasound photoacoustically, or allow a laser excitation to generate a photoacoustic response from the tissue under examination. Such implementations are also compatible and can conceivably be co-packaged with our EPSoC solution.

The remainder of this paper is organized as follows: Section II provides an overview of the MRR based ultrasound sensing principle, and the system architecture, from the wavelength division multiplexed (WDM) interrogation to the dual-chip remoted receiver sensing scheme. Section III analyzes the circuit design choices and implementation details of the sensing unit. Section IV experimentally demonstrates the functionality of the ASIC, including single-cell and full array results, while Section VI concludes the paper and outlines future directions.

# II. SYSTEM ARCHITECTURE

# A. MRR-based Ultrasound Sensors

Fig. 2(a) illustrates an MRR, which consists of a circular waveguide coupled onto a bus waveguide. Destructive interference occurs at the output of the bus waveguide (thru port) when the input light wavelength is such that the accumulated phase shift around the ring waveguide is an integer multiple of  $2\pi$ . In that case the power circulating in the ring is maximized, the MRR is said to be on-resonance, and a notch can be seen in the transmission spectrum of its thru port in Fig. 2(b).

To use this resonant structure as an ultrasound sensor, the incoming pressure waves need to sufficiently modulate the resonant wavelength. This modulation directly translates to a

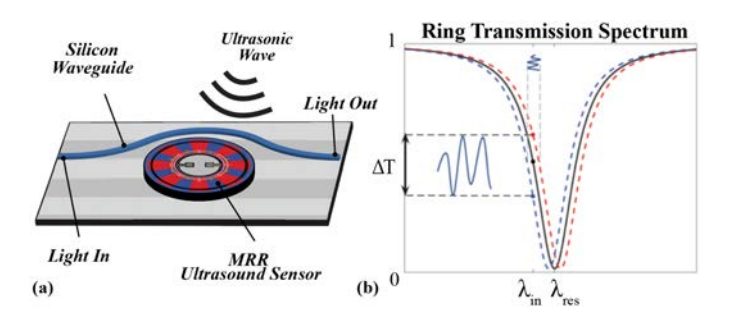


Fig. 2. (a) Graphic representation of a micro-ring resonator MRR. (b) Amplitude transmission spectrum of the MRR indicating the resonant shift based sensing principle.

change in the transmitted optical power at the thru port of the resonator and is maximized if the wavelength of the input light,  $\lambda_{in}$ , matches the maximum slope point of the Lorentzian transfer function of Fig. 2b. This ultrasound induced signal can subsequently be read out electrically using a photodetector and a transimpedance amplifier (TIA). The sensitivity of the entire system can be written as:

$$S = \frac{\partial V_{out}}{\partial T_{app}} = \frac{\partial \lambda_{res}}{\partial T_{app}} \frac{\partial P_{thru}}{\partial \lambda_{res}} H_{PD} G, \tag{1}$$

where the S is the system sensitivity in [V/Pa],  $V_{out}$  is the voltage at the TIA output,  $\lambda_{res}$  is the resonant wavelength,  $T_{app}$  is the applied ultrasound pressure,  $P_{thru}$  is the thru port optical power,  $H_{PD}$  the photodetector responsivity, and G the transimpedance gain of the TIA.

Defining the first two terms of Eq. (1) as *intrinsic*,  $S_{int}$ , and *photonic*,  $S_{phot}$ , sensitivities respectively we can additionally write that:

$$S_{int} = \frac{\partial \lambda_{res}}{\partial T_{app}} = \frac{n_{eff}}{n_g} \left( \frac{\lambda_{res}}{n_{eff}} \frac{\partial n_{eff}}{\partial T_{app}} + \frac{\lambda_{res}}{L} \frac{\partial L}{\partial T_{app}} \right), \quad (2)$$

$$S_{phot} = \frac{\partial P_{thru}}{\partial \lambda_{res}} \approx P_{thru} \frac{1}{FWHM} = P_{thru} \frac{Q}{\lambda_{res}}, \quad (3)$$

where  $n_{eff}$  is the refractive index,  $n_g$  is the group index, L is the ring circumference, FWHM the resonator full width at half maximum, and Q the quality factor of the MRR. In deriving Eq. (2),  $n_g$  accounts for dispersion, while in Eq. (3) full extinction and linear operation around  $\lambda_{in}$  have been assumed. The *intrinsic* sensitivity,  $S_{int}$ , is a measure of the platform's suitability to sense ultrasound and depends primarily on the device materials and geometry [28]. On the other hand, the *photonic* sensitivity,  $S_{phot}$ , primarily depends both on photonic design and technology with Eq. (3), highlighting the importance of high-Q MRR sensors. High sensitivity devices with  $Q = 2 \times 10^5$ , have been demonstrated in our zero-change platform [29], indicating its suitability for ultrasound sensing. A more detailed sensitivity analysis of MRR based biosensors is provided in [30].

# B. Remoted WDM Dual-Chip Optical Ultrasound

The proposed remoted optical ultrasound sensing scheme is illustrated in Fig. 3 (a) for a single sensor-receiver pair. Initially, the *PD-MRR* resonance is matched to the wavelength of the incoming laser light, using a digitally controlled thermal tuning locking loop. This ensures maximum PD-MRR responsivity since most of the available optical power circulates in the ring when on resonance. Subsequently, the heater code of the *sensor MRR* is swept and its Lorentzian is captured using the *PD-MRR*, as shown in Fig. 3 (b). To maximize this sensing scheme's sensitivity, the *sensor MRR* is resonance controlled to guarantee that the maximum slope point of its Lorentzian is aligned to the input laser wavelength.

This concept can be extended to multiple sensor-PD MRR pairs. Combining optical MRR-based transducers with active resonance tuning offers the capability of simultaneously interrogating multiple MRRs coupled onto the same waveguide in a WDM fashion using a fixed wavelength multiple channel comb laser, as presented in Fig. 4. This translates to a reduction of I/O fiber channel count proportional to the number of optical modes available on the comb laser with zero power and area overhead. In this first generation EPSoC, 8 MRRs are coupled onto the same waveguide. Simple 8-channel integrated multiwavelength laser diodes have recently been reported [31] and could be used with this EPSoC, further simplifying the overall system and minimizing its form factor, while  $16-\lambda$  combs are also available [32], leading to even higher fiber-count reduction. The concept of WDM interrogation of multiple MRRs coupled onto the same waveguide is shown in Fig. 4.

Lastly, a dense 2-D MRR sensor matrix can be implemented by arraying multiple identical WDM ring rows in parallel on a sensor EPSoC. Utilizing an area efficient multi-mode interferometric (MMI) splitter tree, the comb laser input is distributed into the WDM row replicas. Splitting the optical power on chip further reduces the cable count, allowing us to interrogate the entire 2-D array with a single input fiber. The conceived system architecture implemented on this EPSoC is shown in Fig. 5. A sensor chip containing only an MMI splitter tree, high *Q*-factor (and consequently high sensitivity)

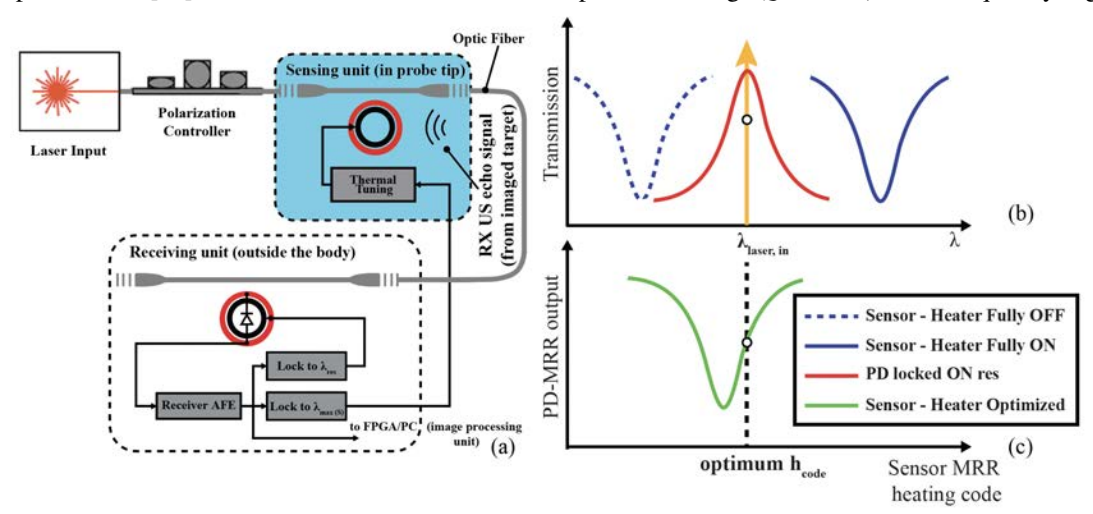


Fig. 3. (a) Remoted optical ultrasound sensing scheme, illustrating the location of sensing and receiving units. (b), (c) Optimization of PD and sense MRR heater codes for remote ultrasound sensing. After an initial calibration step, the heating code of the sensor ring is set such that it is biased on the stable side of the ring Lorentzian. The PD ring's resonance is locked onto  $\lambda_{in}$ , such that the circulating power in the ring, and thus the responsivity is maximized.

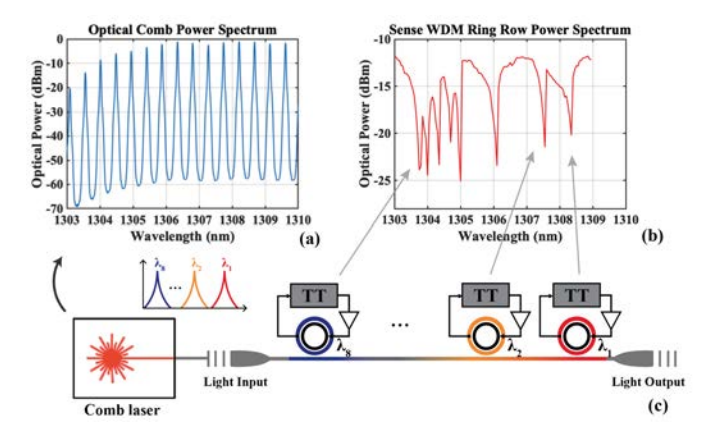


Fig. 4. Illustration of the need for active resonance tuning for WDM interrogation. Measured optical power spectrum of: (a) the available comb laser, (b) an on-chip sensor WDM ring row spectrum before tuning. (c) Schematic representation of a WDM ring row consisting of multiple MRRs coupled onto the same silicon waveguide and interrogated by a comb laser input.

sense MRRs and thermal tuning circuitry is placed at the probe tip, where power and area minimization are critical, while a receiver chip with PD-MRRs, analog receivers, digital tuning control logic, and serialization, recovers the ultrasound signal and sends it to an FPGA that performs beamforming and image processing.

To prove the remoted ultrasound concept in a single tapeout, the implemented prototype EPSoC is designed to be configured either as a sensing or as a receiving chip. Also, in order to enable monitoring and debugging of the tuning loops of the sensor MRRs and to streamline the design process, the same mixed-signal block is used to interface with both the sense and PD MRRs constraining the pitch to  $220\mu m$ . This should be sufficient to enable a  $180^{\circ}$  field of view (FOV) at 3.6 MHz and  $> 85^{\circ}$  FOV at 5 MHz, without the formation of grating lobes. However, the sensing area that will eventually be required is  $< 0.01 mm^2$  per sensing element, as proved by the performed experiments. This translates to a much higher sensor density and an FOV of  $180^{\circ}$  up to 15 MHz, assuming a sensor pitch of  $50 \mu m$ .

Quantifying the integration density that an optical sensor approach offers, fiber assemblies with 61 channels packaged

in  $330\mu m \times 280\mu m$  area have been reported [33]. Combined with a high input power comb laser we can use an MMI splitter tree to split a single input into 60 ring rows on-chip. Assuming 16 MRRs per WDM row, 960 sensors can be simultaneously interrogated with a 2.8mm diameter fiber bundle [34]. This is in stark contrast to the high-density microcoax cable counterpart where only 192 cables can fit in a 7.5mm diameter bundled cable [35].

## III. RECEIVER UNIT IMPLEMENTATION

Fig. 6(a) shows the schematic of a receiver unit cell. It consists of a dedicated mixed-signal block for each sensor, with a TIA, followed by a pre-amplifier and a 9-b successive approximation register (SAR) ADC that digitizes the received ultrasound signal at 50MSa/sec. The outputs of 4 blocks are then serialized and transmitted to an FPGA for post-processing using a current mode logic (CML) output stage that ensures sufficient signal swing.

# A. System Specifications

As it propagates through tissue, ultrasound is attenuated due to both scattering and absorption. Absorption, which is the dominant loss mechanism, has an attenuation coefficient of  $\sim 1 \mathrm{dB/cm/MHz}$  [36] in soft tissues. This implies that ultrasound echo signal strength will be heavily depth and scattering dependent, necessitating a wide dynamic range (DR) on the order of 70-80 dB. To meet this requirement, variable frontend gain is often employed in a time-gain control scheme [37]. In this work, we utilize a tunable resistor network and bleeder I<sub>DACS</sub> to carry out mode switching and time-gain control.

The wide DR needs to be combined with a low noise equivalent pressure (NEP) such that images from high depths can be reliably taken. The integrated NEP of a system can be calculated as a function of the sensitivity, S, and the integrated noise, N, over the bandwidth of the system (which should be equal to the bandwidth of the signal of interest to filter out high frequency noise), where both S and N are estimated at the same point in the transduction chain. Referring the current noise density at the input of the TIA,  $\overline{i_n^2}$ , back to pressure

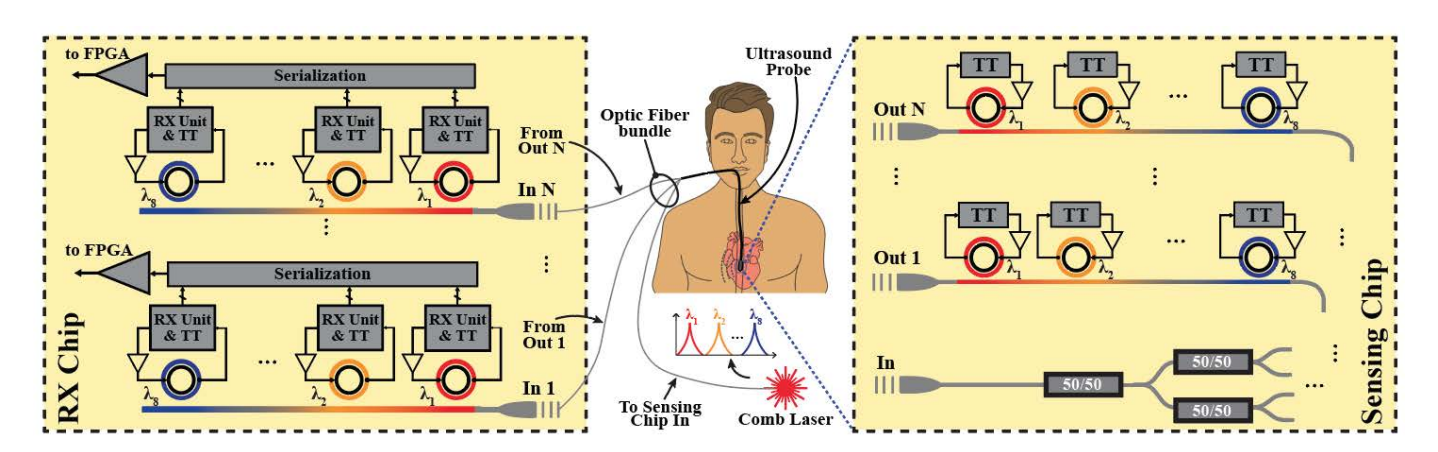


Fig. 5. Dual-chip system architecture illustrating the remoted optical ultrasound beamforming array concept for power and area minimization.

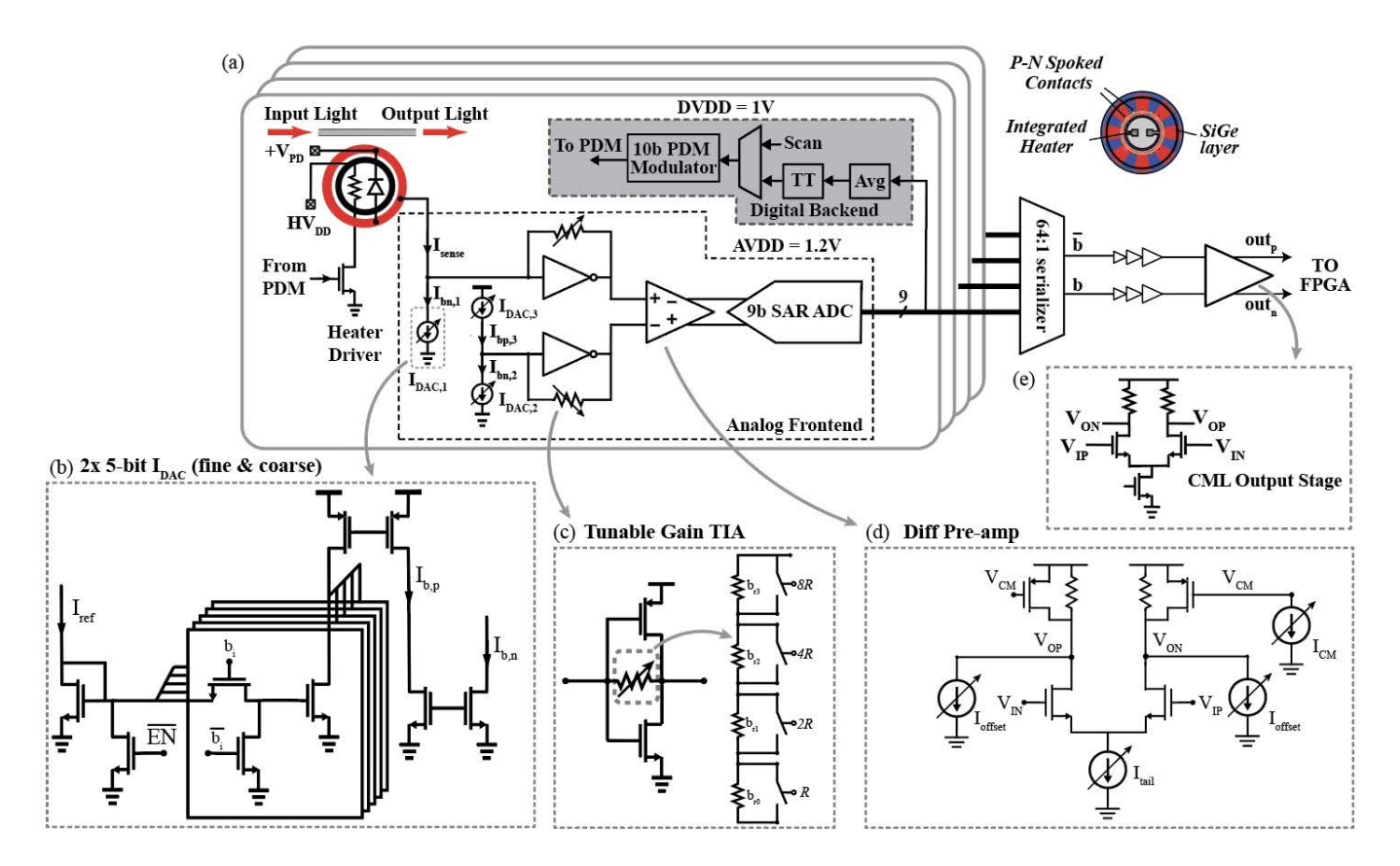


Fig. 6. Receiver quad schematic with details of the mixed signal block and the serialization and output stage - Edited.

through the intrinsic and photonic sensitivities (Eqs. 2, 3) we obtain:

$$NEP = \frac{N}{S/G} = \frac{\sqrt{\overline{i_n^2} \cdot BW}}{S_{int} \cdot S_{phot} \cdot H_{PD}}.$$
 (4)

A NEP target of  $\sim$ 1kPa will ensure imaging depths down to 5-6 cm are comfortably achieved using a TX ultrasound transducer like the one in [8]. Additionally, a low NEP value can enable use of this sensor in alternative modalities where the received signal is of much lower amplitude, such as photoacoustic imaging.

# B. Analog Front-End

To ensure the NEP specification is met, an MRR with high intrinsic sensitivity had to be combined with a lownoise analog front-end receiver. At the same time, the high DR dictates a topology with sufficient headroom, even though this can be relaxed with the inclusion of gain programmability.

An inverter-based TIA with resistive feedback shown in Fig. 6(c) is used in the core of this front-end to convert the sensor input signal from the current to the voltage domain for further processing. It combines low noise performance with high DR, while maintaining high BW, with the the additional benefits of design simplicity, area minimization, and current efficiency, [6], [38]. This topology achieves comparable noise performance for the required dynamic range to other popular solutions such as the common-gate TIA [39], [40] or the capacitive feedback TIA [41], [42] which were not selected

due to headroom (DR) and area considerations respectively [6].

Gain programmability of 24 dB in 6-dB steps is implemented with the use of a 4-bit binary-weighted resistive network (Fig. 6(c)) that is digitally controlled through scan and allows for fast and easy switching between different modes of operation. The resistor values range from  $50k\Omega$  to  $800k\Omega$ , which ensures that the resistor thermal noise is negligible, even for the lowest gain setting. Additionally, a pseudo-differential scheme with a dummy replica path was utilized as shown in Fig. 6(a) to enhance the power supply rejection ratio (PSRR) of the AFE.

To ensure the TIA output is not saturated at high input optical power or high gain operating mode, the DC background photocurrent of the PD-MRR must be precisely cancelled. To this end, three IDACs following the topology shown in Fig. 6(b) were generated using the Berkeley Analog Generator (BAG) [43]. They have a global enable and the output can be configured to be push or pull (Iout,n or Iout,p) by specifying the corresponding parameter in the layout generation code. The dummy TIA has two 3-bit push-pull I<sub>DAC</sub>s, while the sensing TIA a 10-bit pull IDAC separated in 5-bits of fine and 5-bits of coarse tuning, with nominal LSBs of 4µA and 120nA respectively. This fine I<sub>DAC</sub> LSB ensures that the output common-mode voltage can be tuned with a step < 0.1 V for the highest gain setting (800k $\Omega \cdot 120$ nA). The coarse I<sub>DAC</sub> has a minimum step of 4µA, and can be used to switch between different modes of operation. During this switching the input optical power, and consequently  $S_{phot}$ , are adjusted so that stronger or weaker signals can be detected. In such scenarios, the value of the background current that needs to be cancelled should be accordingly adjusted.

Subsequently, a low-gain (6dB) preamplfier was used to perform single-ended to differential conversion and ensure that any offset due to mismatches in the DC current or feedback resistor values of the main and dummy TIA stages is cancelled out. The preamplifier schematic is shown in Fig. 6(d): it can both adjust the common mode input voltage to the SAR ADC to ensure maximum headroom and cancel the offset of the first amplification stage. Output CM control is performed by a diode-connected device controlling the gates of PMOS bleeders with 3-b programmability, while single-bit offset correction is done through NMOS bleeders connected to the amplifier output.

A 9-bit asynchronous successive approximation register (SAR) ADC, implemented using BAG and Laygo [44], digitizes the downconverted ultrasonic data. In these experiments, running the SAR at 50MSa/sec is sufficient to ensure a delay resolution of 20ns and a sampling rate well above Nyquist for a 5MHz ultrasonic input. The number of ADC bits was selected such that the quantization noise does not dominate the noise budget. With 9 bits, the input referred quantization noise will be comparable to the worst case thermal noise from the feedback resistor. At the same time, even though a lower ADC sampling rate can be used to lower the power consumption, this benefit is minimal, and clock rate (and consequently the ADC rate) is tied to the thermal tuning control loop through fixed, non-programmable divider ratios. The BW of that loop needs to be below the ultrasonic signal frequency to avoid canceling it, but above the ring thermal time-constant to actively cancel any environmental disturbance to the resonant wavelength.

To reduce the number of required output pads the digitized signals of 4 adjacent receivers are then serialized using a 64-to-1 mux-latch-tree serializer, with a 28-bit preamble sequence that allows data packet alignment on the FPGA. This grouping and serialization of the digital outputs is shown in Fig. 6(a).

A CML driver with load resistance  $R_L$ , is the final output stage as shown in Fig. 6(e). The transistors of this diff-pair are sized to provide sufficient differential swing for gigabit receivers on the FPGA assuming  $50\Omega$  termination and speeds

up to 6.4GHz. To drive the large input capacitance of the CML output stage, digital buffers have been placed between the output of the serializer and the CML driver's input. While this power hungry CML output stage can be replaced with a low power LVDS link [45] in future implementations, design simplicity and robustness were preferred in this first EPSoC prototype, seeing as power minimization on the receiver chip was not a primary concern since it resides outside the body.

## C. Noise Analysis

The main noise contributors at the input of the receiver unit will be shot noise, thermal noise from the bleeder  $I_{DAC}s$ , the feedback resistor, and the input MOSFETs, as well as quantization noise from the ADC. Of those, only the first three significantly contribute to the overall noise budget and are mathematically described as:

$$\overline{i_{n.shot}^2(f)} = 2qI_{PD} = 2qH_{PD}P_{circ}, \tag{5}$$

$$\overline{i_{n,th,I_{DAC}}^2}(f) = 4kT\gamma g_{m,eff},^{1}$$
 (6)

$$\overline{i_{n,th,R_f}^2}(f) = \frac{4kT}{R_f},\tag{7}$$

where  $q=1.6\cdot 10^{-19}\mathrm{C}$  is the unit charge,  $I_{PD}$  is the photodetector current,  $H_{PD}$  is the photodetector responsivity,  $P_{circ}$  the optical power circulating in the PD-ring, k Boltzmann's constant, T the temperature,  $\gamma$  the MOSFET white noise parameter,  $g_{m,eff}$  the "effective"  $I_{DAC}$  transistor transconductance, and  $R_f$  the TIA feedback resistor. These

 $^{1}g_{m,eff}$  represents an "effective" transconductance, used to lump the thermal noise of all the transistors of the  $I_{DAC}$ s in one parameter, and can be extracted through simulation.

TABLE I
TYPICAL AND SIMULATED RECEIVER UNIT PARAMETERS – NEW TABLE

Parameter	Value			
$H_{PD}$	0.5A/W			
$C_{PD}$	30fF			
$\gamma$	2/3			
$g_{m,eff}$	1.7mS			
$R_f$	$(50-800) \text{ k}\Omega$			

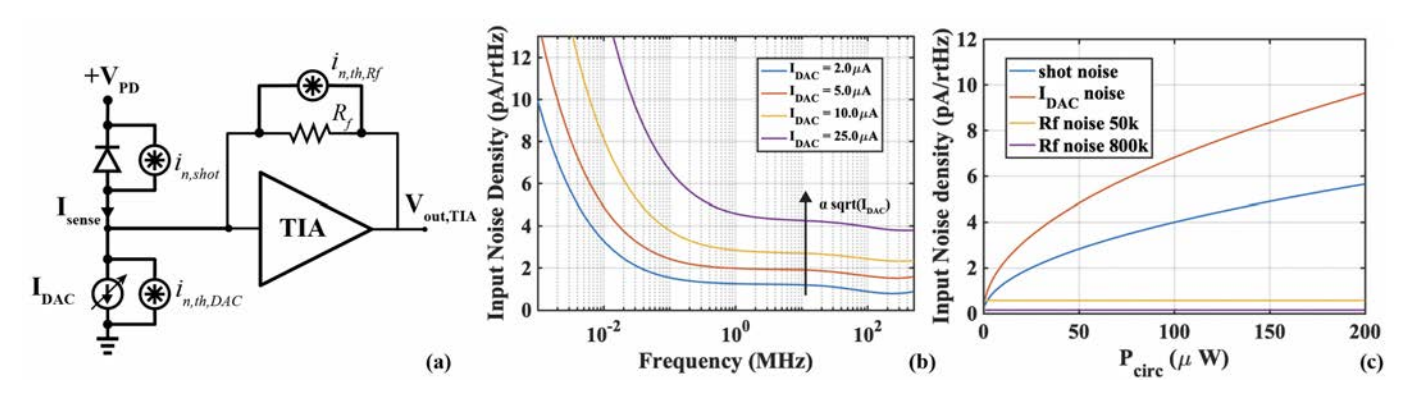


Fig. 7. (a) Simplified AFE schematic indicating the main noise sources, (b) Noise simulations for various  $I_{DAC}$  settings, (c) Input noise densities vs  $P_{circ}$  for different noise sources (right).

main noise contributors are depicted in Fig. 7(a). At the same time, the sensor input signal,  $I_{sense}$ , can be written as:

$$I_{sense} = S_{int}S_{phot}H_{PD}T_{app} = S_{int}P_{opt}\frac{Q}{\lambda_{res}}H_{PD}T_{app},$$
(8)

Noise simulations of the TIA and preamplifier, for different I<sub>DAC</sub> settings, are presented in Fig. 7(b). These simulations used the parameter values tabulated in Table I. Fig. 7(b) plots various noise contributions as a function of the power circulating in the ring,  $P_{circ}$ , assuming  $H_{PD} = 0.5$ A/W, indicating that the front-end is shot-noise limited. Given that the bleeder  $I_{DAC}$  needs to cancel the photocurrent  $I_{DAC}$   $\propto$  $I_{\rm PD} \propto P_{circ}$ , it can be considered "shot-noise", even though it is thermal in nature. Indeed the input noise density floor increases proportionally to  $\sqrt{I_{DAC}}$  in Fig. 7(b), indicating that feedback resistor, input MOSFETs, and ADC quantization noise are negligible. Also, note that Fig. 7(c) a lower  $R_f$  could be used to enable larger input signals as long as the  $R_f$  and quantization noise remain non-dominant. However, the same exact effect can be achieved by lowering the input optical power, which would lower the sensed input current,  $I_{sense}$ according to Eq 8..

The simulated total noise, integrated over an 80% fractional BW around 5MHz is  $\sqrt{I_{n,tot}^2} \simeq 10.36 \mathrm{nA}$ . At the same time, using Eq. 8, and  $T_{app} = 1 \mathrm{kPa}$ , we obtain  $I_{sense} = 15.4 \mathrm{nA}$ , indicating that our design should meet the target NEP specification.

To calculate the theoretically expected simultaneous electronic DR, the maximum current that does not saturate the ADC needs to be found. The simulated full-scale range of the ADC is 0.6V, which can be referred back to the TIA input using the minimum  $R_fG_{preamp}$  setting as:  $I_{sat}=0.6V/(2\cdot50\mathrm{k}\Omega)=6\mu\mathrm{A}$ . Hence, the DR<sub>el</sub> is:

$$DR_{el} = 20 \log \left( \frac{\frac{1}{2\sqrt{2}} I_{sat}}{\sqrt{\overline{I_{n,tot}^2}}} \right) = 46.2 dB.$$
 (9)

However, the sensor dynamic range will be limited by the ring linear region, which is  $\sim\!\!FWHM$ . At such high pressure levels, the incident optical power to the ring can be reduced to avoid saturation while the fine  $I_{DAC}$  resolution properly cancels out the background current at low gain settings. The sensor DR is then defined as the maximum pressure that does not saturate the ring Lorentzian over the minimum detectable pressure. Given that  $NEP = \sqrt{I_{n,tot}^2}/(H_{PD}S_{phot}S_{int}) = 935Pa$ , and that  $T_{app,max} = FWHM/S_{int} = \frac{130pm}{40fm/kPa} = 3.25MPa$ , we can write:

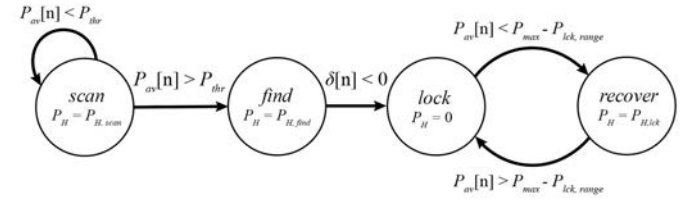
$$DR = 20 \log \left(\frac{T_{app,max}}{NEP}\right) = \frac{P_{opt}H_{PD}}{\sqrt{\overline{I_{n,tot}^2}}} \simeq 73.7 dB. \quad (10)$$

Eq. 10 shows that the DR can be improved by increasing the optical power incident upon the ring or by using more efficient photodetectors to lower the NEP.

## D. Digital Back-End

Resonance control is achieved on this EPSoC by wrapping an active thermal tuning feedback loop around the ring. As

#### PD-lock Mode Controller



#### Sense-lock Mode Controller

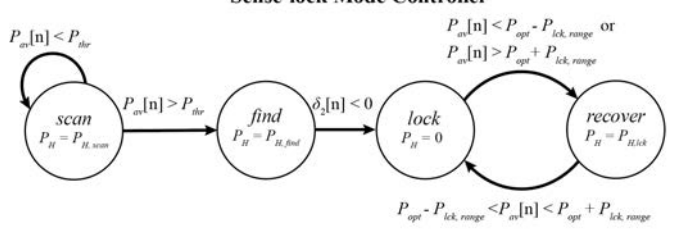


Fig. 8. State-chart of the controller FSM in PD-lock and Sense-lock modes.

shown in Fig. 6(a) the averaged SAR output is fed into a digital feedback loop which produces a 10-b heat code input to a pulse density modulator (PDM). The PDM is comprised of a 10-b accumulator whose carry out controls the gate of an NMOS switch in series with a resistive heater embedded in the ring cavity, also depicted in Fig. 6(a). Alternatively, the 10-b PDM input can be externally set through scan, to ensure the heater can be programmed in case the controller does not work as intended.

Thermal tuning is the only method to provide the required tuning range compared to other alternatives such as carrier-depletion [46] or carrier-injection [47]. To ensure that the controller will only be cancelling thermal variations and not the incoming ultrasound signal, all digital tuning logic needs to be running faster than the thermal time constant of the ring (30 $\mu$ s) but slower than the signal of interest (here 3MHz, assuming an 80% fractional BW around 5MHz). Here, the averaged output of the ADC updates the controller at  $\approx$ 98kHz.

Depending on whether the ring is intended to be used as a power detector or as a sensor its resonance needs to lock either precisely onto the input wavelength, or slightly offset from it, such that the sensitivity is maximized. This necessitates two controller operation modes, PD-lock, and Sense-lock, both described by an FSM with 4 different states: "scan", "find", "lock", and "recover". Fig. 8 presents a state-chart diagram of the decision process of the FSM where the following nomenclature is used:  $P_{av}[n]$  indicates the averaged SAR output, and  $P_H$  is the heating step by which the PDM is incremented. We will also refer to the resonant wavelengths without and with thermal tuning applied as  $\lambda_{res,0}$ , and  $\lambda_{res,h}$  respectively.

The controller begins the search from the *scan* state, assuming that  $\lambda_{res,0} < \lambda_{in}^2$  for both modes of operation. In this state the light circulating in the ring is minimal, and the output of the ADC (and the averaging block) is low. The controller

 $<sup>^2\</sup>lambda_{in}$  refers to a fixed wavelength optical input. This condition can be satisfied by charting the relative position of the resonance to the optical input in a "bring-up" calibration step and then accordingly initializing the PDM.

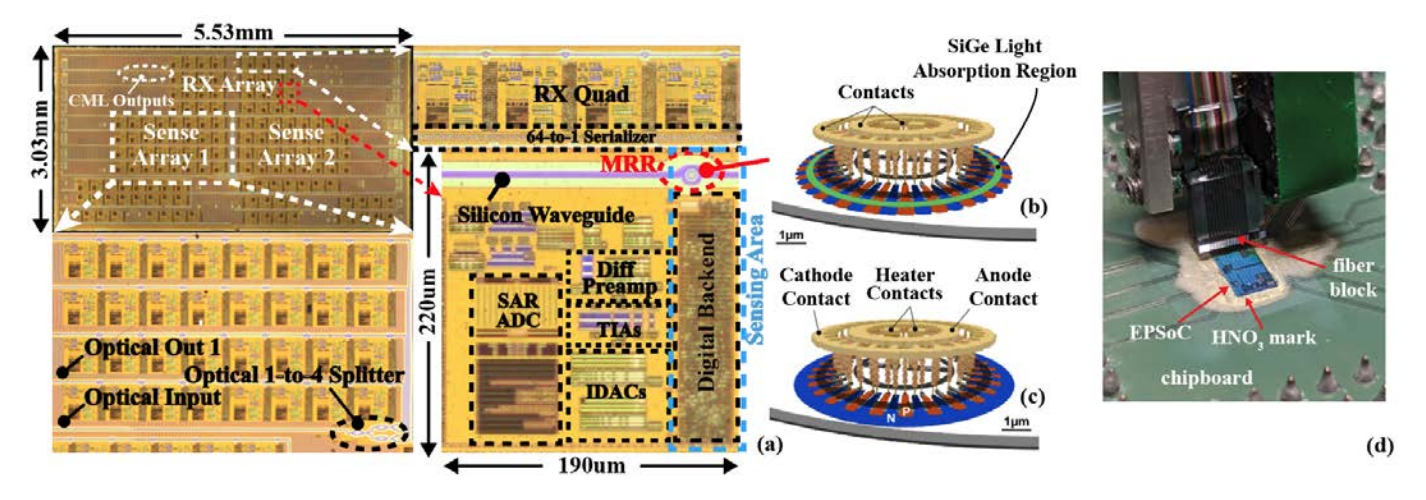


Fig. 9. (a) Die photo with insets of an 8x4 sensing MRR array, a receiver PD-MRR quad and a sensing unit. (b), (c) 3-D layout renderings of PD and sense MRRs respectively (from [48]). (d) 12-channel fiber block mounted on a 6-axis nano-positioning stage ready to be aligned and attached on an EPSoC with substrate released and sidewall epoxy etched.

 $\begin{tabular}{l} TABLE \ II \\ POWER \ AND \ AREA \ BREAKDOWNS FOR THE RECEIVER \& SENSING UNITS \\ \end{tabular}$ 

	Power (mW)	Area (mm <sup>2</sup> )
AFE	2.63	0.034
CML Output Stage	5.25	0.007
Serializer	0.14	0.025
Digital BE	0.13	0.098
PDM Driver & MRR Heater	0.3	0.002
Sensing Unit*	0.43	0.01
Total	8.45	0.076

<sup>\*</sup> Text in blue refers to sensing unit blocks

will keep incrementing the PDM by a coarse step,  $P_{H,scan}$  until the averaged output,  $P_{av}[n]$ , crosses a programmable threshold,  $P_{thr}$ , which will indicate that  $\lambda_{res,h}$  is close to  $\lambda_{in}$ , and move the FSM into the "find" state where the PDM step is decremented to a finer value,  $P_{H,find}$ . In this state the first and second order difference between consecutive readings of the averaging block,  $P_{av}[n]$ , are monitored. These are defined as:

$$\delta[n] = P_{av}[n] - P_{av}[n-1], \tag{11}$$

$$\delta_2[n] = \delta[n] - \delta[n-1] = P_{av}[n] - 2P_{av}[n-1] + P_{av}[n-2].$$
(12)

The heating codes at which the sign of  $\delta[n]$  or  $\delta_2[n]$  changes correspond to  $\lambda_{in}$  aligned with the resonance or the maximum slope of the Lorentzian respectively. The outputs of the averaging block at those input codes are labeled  $P_{max}$  and  $P_{opt}$  respectively. The controller subsequently enters the "lock" state, and the PDM is no longer incremented. A configurable dead-zone around  $P_{max}$  and  $P_{opt}$  is defined by  $P_{lck,range}$  to avoid unnecessary dithering. If the ring drifts outside that region it enters the "recover" state, where a  $P_{H,lck}$  step is applied to ensure it can recover.

Note that  $P_{thr}$ ,  $P_{H,scan}$ ,  $P_{H,find}$ ,  $P_{H,lck}$ , and  $P_{lck,range}$  can be adjusted for the controller to work for different values of incident optical power and AFE gain.

#### IV. EXPERIMENTAL RESULTS

Fig. 9(a) presents a micrograph of the EPSoC, with insets into a receiver PD-MRR quad and a sensing unit. 3-D renderings of the PD and sense MRRs are also shown in Fig. 9(b), (c) respectively. The EPSoC was fabricated in 45nm CMOS-SOI and occupies a total area of  $3.03\times5.03\text{mm}^2$ . Each sensing unit takes up  $190\times220\mu\text{m}^2$  and consumes 8.45mW of power when the CML output stage is taken into account. To streamline the design the same sensing unit has been abutted to both sensing and receiver rings, restricting the pitch to  $250\mu\text{m}$ . However, only the area taken up by the digital back-end and heater driver is required for the resonance controller to work, indicated in Fig. 9(a) as sensing unit area. That area amounts to  $0.01\text{mm}^2$ , while the required power consumption per sensing unit is 0.43mW. The analytic power and area breakdowns are shown in Table II.

# A. Electronic-Photonic Packaging

Harnessing the capabilities of this monolithic integration platform requires a packaging technique that can enable simultaneous electrical and photonic connectivity. To achieve this, the EPSoC is flip-chip packaged onto a high-density printedcircuit board (PCB), and the silicon handle is removed in a single XeF<sub>2</sub> post-processing dry-etch step, to optically enable the chip for electrooptic measurements. In this prototype, a 12-channel 250µm pitch fiber assembly (OzOptics) was used to simultaneously couple light on the sensing and receiving arrays. Since the fiber block assembly used in this work is wider than the chip, the residual epoxy underfill sidewall had to be removed by means of a HNO3 wet etch to allow attaching the fiber block assembly with reasonable optical coupling losses. A fiber block assembly prior to attach on a substrate released EPSoC is shown in Fig. 9(d). Even though more efficient fiber packaging options have been reported in literature and are compatible with this technology [33], [49], the solution presented provides an easy in-house solution for quick and inexpensive prototype measurements. Lastly, to enable transducer immersion under water while insulating the

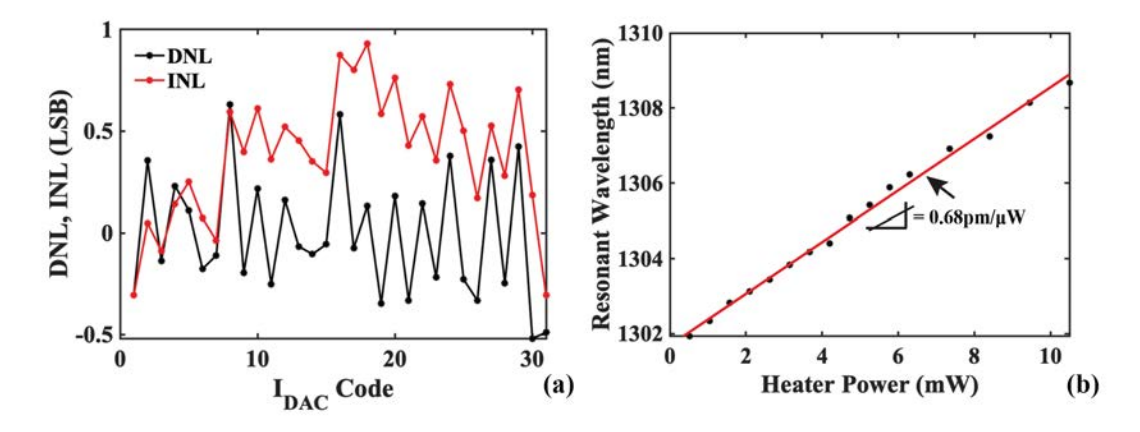


Fig. 10. (a) Extrapolated INL-DNL curves of the SAR ADC, (b) Thermal tuning efficiency measurement.

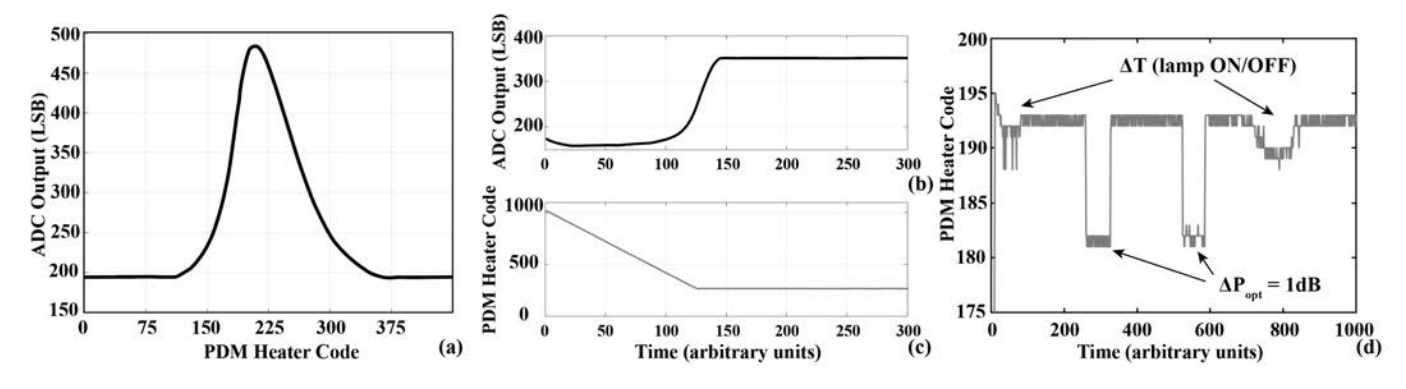


Fig. 11. Thermal tuning controller in action: (a) Lorentzian calibration sweep, (b), (c) ADC output and PDM heating code as the controller achieves and retains lock to the maximum slope, (d) PDM heating code varying to retain lock under laser power, and temperature fluctuations.

rest of the test equipment, a 3-D printed tank was attached over the high-density chip-board using silicone.

# B. Electro-optical Characterization

To verify the correct operation of the AFE, the static transfer function of the SAR ADC is captured by sweeping the fine  $I_{DAC}$  current at the lowest gain setting,  $R_f=50\mathrm{k}\Omega$ . An interpolated INL and DNL estimation is extracted in Fig. 10(a) using the 32 available datapoints at the output of the ADC. An INL of within  $\leq 0.9$  LSB and a DNL of  $\leq 0.6$  LSB are recorded. The gain and resonance tuning capability along with the linear relationship between the recorded Lorentzian slope at the ADC output and the AFE gain have already been verified in [50].

The tuning efficiency of the embedded ring heater was measured by sweeping the heating code of the PDM while monitoring the resonant wavelength shift and current drawn from the heater supply. As expected, the resonant shift varied linearly with the heater power, with a fitted slope of 0.68pm/µW shown in Fig. 10(b). This high tuning efficiency is a benefit of the monolithic integration of electronics and photonics, and a key system attribute in achieving ultra-low power consumption per sensing element.

Lastly, the operation of the resonance tuning controller was examined. Initially, a CW laser input was parked slightly above the unheated ring resonance as assumed in Section III-D. Then

the thermal tuner was allowed to run and achieve lock. Due to noise in the averaged ADC output, a flip of the sign of  $\delta[n]$  in Eq. 11 occurred before the resonance,  $\lambda_{res,h}$ , crossed the input wavelength  $\lambda_{in}$ . The same holds true of the sign of  $\delta_2[n]$ , in Eq. 12. This meant that the controller left the *find* state and entered the *lock* state almost right after crossing the threshold,  $P_{thr}$ , regardless of the mode of operation, PD-lock or Sense-lock.

To circumvent this, an initial calibration of the Lorentzian was run, where the averaged ADC output value that corresponded to the maximum slope or the resonance was determined as shown in Fig. 11(a). Then, the threshold  $P_{thr}$ , was selected to match that value and the controller was allowed to run and acquire lock as shown in Fig. 11(b)–(c). Additionally, Fig. 11(d), illustrates that the controller adjusts the PDM value to retain lock when a microscope lamp is turned ON and OFF over the chip, resulting in mK changes in temperature, and when the input laser power is varied by 1dB.

## C. Single PD-MRR sensor

To evaluate single sensor performance a PD-MRR was used as both a sensor and a receiver. A CW laser was parked at the stable side of the PD-MRR Lorentzian, and the EPSoC was insonified by a commercial piezoelectric transducer (Olympus, A310S-SU, flat 5MHz center frequency). The spectrum of a sinusoidal excitation at 5MHz is shown in Fig. 12(a). At

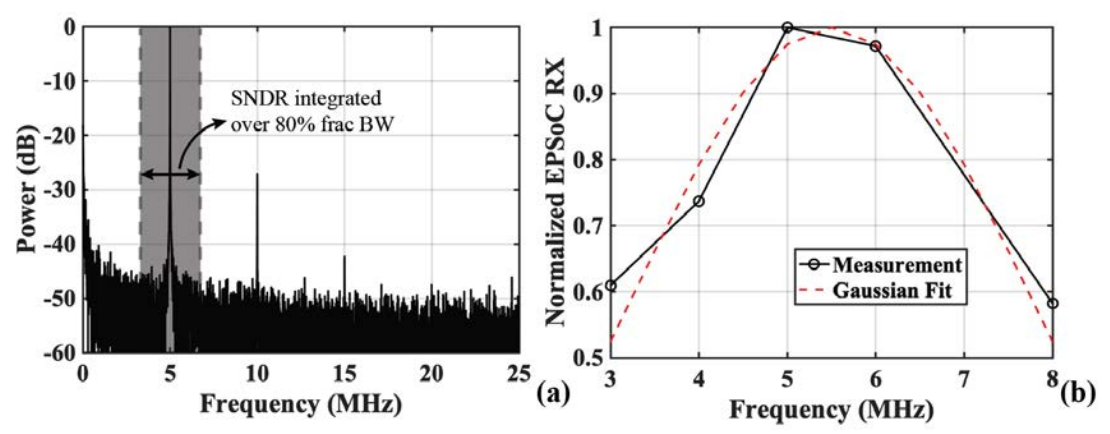


Fig. 12. Power spectrum of the PD-MRR -6dBFS response to a 5MHz tone input, (b) Normalized EPSoC transfer function for the same PD-MRR site.

the highest acquired amplitude, which was -6.7 dBFS (234 LSB<sub>pp</sub>), an SNDR of 25.5dB was measured at a gain setting of 700k $\Omega$ . The SNDR was estimated by integrating the noise over an 80% fractional BW around 5MHz.

Extrapolating to the lowest gain setting of  $R_f = 50 \mathrm{k}\Omega$  we can expect an SNDR of 48.4 dB at higher input pressure waves, very close to the theoretically expected value. This value has not been confirmed experimentally since the available transducer could not produce a high enough input signal to saturate the ADC at lower gain settings. In fact, the harmonic distortions seen in the noise spectrum of Fig. 12(a) originated from the piezo transducer's non-linearity. The increase of the noise spectrum around 1MHz, can be explained by 1/f noise kicking in, a phenomenon which can also be seen in the simulated noise densities in Fig. 7(b). Both the harmonics, and this low frequency noise do not pose a practical problem, since they can be filtered out during post-processing.

The integrated noise at the output of the ADC in LSBs can be calculated as:

$$SNDR = 20 \log \left( \frac{\frac{1}{2\sqrt{2}} V_{amp,pp}}{N} \right)$$
 
$$N = \frac{V_{amp,pp}}{2\sqrt{2} \cdot 10^{SNDR/20}} = 4.4 \text{ LSBs}.$$

This noise can be referred to the input, to calculate both  $I_{n,tot}$  and NEP. The gain used in this experiment was  $R_f = 700 \mathrm{k}\Omega$ , while the measured parameters relevant for  $S_{phot}$  calculation were Q=6000,  $P_{opt}=100 \mathrm{\mu W}$ , and  $H_{PD}=0.2 \mathrm{A/W}$ . These values yield:

$$\begin{split} I_{n,tot} = N \cdot \Delta_{SAR,LSB} \cdot \frac{1}{G_{preamp}R_f} = 4.4 \cdot \frac{0.6}{512} \cdot \frac{1}{2 \cdot 700 \text{k}} \\ = 3.68 \text{ nA}, \end{split}$$

$$NEP = \frac{I_{n,tot}}{S_{int}S_{phot}H_{PD}} = 996 \text{ Pa.}$$

The NEP density can be estimated as  $NEP_{\rm den}=0.498~Pa/\sqrt{\rm Hz},$  in close agreement with the theoretically expected value.

Normalized EPSoC PD-MRR received amplitude and a Gaussian fit corresponding to the transfer function of the piezo transmitter are plotted in Fig. 12(b), indicating the MRR has sufficient ultrasonic BW, around 5MHz. The wide BW of the

device has also been verified in [28], while the sensitivity of the receiver unit was measured to be 7.3 mV/kPa at the  $400 \text{k}\Omega$  gain setting in [50], a value comparable to that of commercially available hydrophones.

# D. Remoted Optical Ultrasound

The setup of Fig. 13(a) was used to prove the remoted ultrasound sensing principle. A PD and sense MRR pair with similar unheated resonant wavelengths  $\lambda_{res,0}$  were selected for this experiment. The resonant wavelength of the PD-MRR was first locked onto a CW laser input parked at a fixed wavelength,  $\lambda_{in}$ , using the tuning controller. Subsequently, the heater of the sensor-MRR was swept, producing the Lorentzian response of Fig. 13(b) that was captured on the ADC output through scan. Finally, the sensor MRR was biased at the optimal heating code, the sensor EPSoC was insonified by the piezoelectric transducer, and the time-domain waveform acquired is plotted in Fig. 13 (c).

To compensate for the high coupling loss of  $\sim 5 \text{dB/coupler}$ , which in this sensing scheme has to be suffered thrice making for 15dB of total attenuation (in & out of sensing chip and in of the receiver chip), a booster optical amplifier (BOA) was used to pre-amplify the CW laser tone. The self heating of the ring due to the high optical input power [51] is the cause of the slope mismatch between the two sides of the Lorentzian in Fig. 13 (a).

The dual-chip scheme outlined in Section II, was not demonstrated for the full sensor-receiver array primarily due to (a) a 7nm ( $\sim$ 1.26THz) mismatch between the nominal values of the central wavelengths,  $\lambda_c$ , of the available comblaser diode and the unheated sensor-MRR WDM row, and (b) a 4nm ( $\sim$ 720GHz) mismatch between the central resonant wavelengths of the unheated sensor-MRR and PD-MRR WDM rows. This issue will be corrected in future tape-outs by properly sizing the MRRs using the data-points from this first prototype to achieve better resonance matching.

# E. Optical WDM RX Beamforming

To demonstrate optical WDM sensing and beamforming, a comb laser diode simultaneously interrogates 8 MRRs. Again, the PD-MRR array serves as both sensor and receiver due to high coupling loss combined with low available input optical

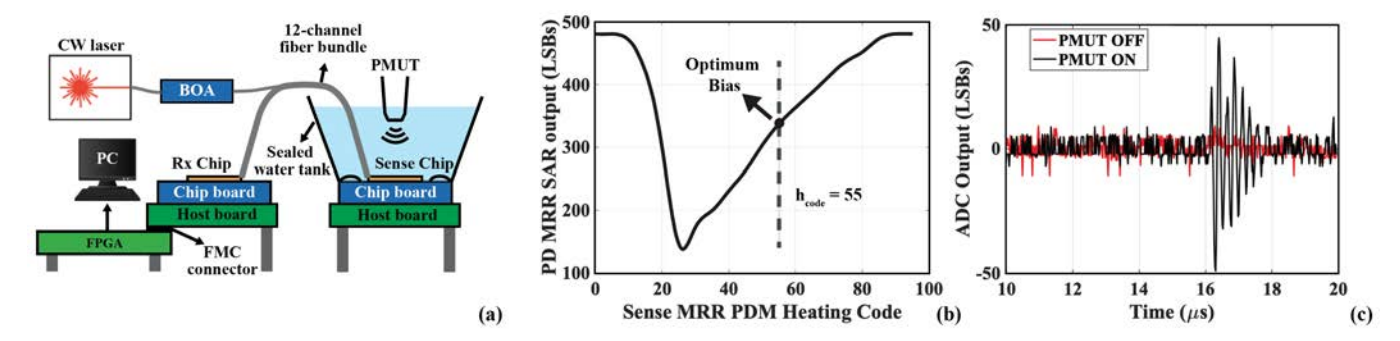


Fig. 13. Remote sense-receive optical ultrasound sensing demonstration: (a) Illustration of the remoted optical ultrasound sensing setup. (b) Sense MRR Lorentzian measured at the output of the PD MRR. (c) Time-domain received waveform with and without insonification.

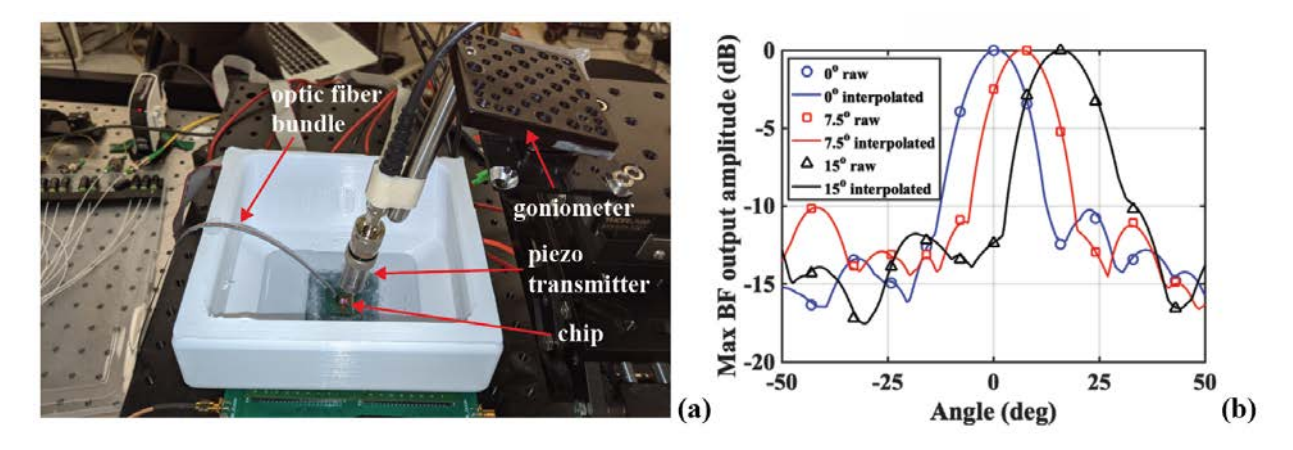


Fig. 14. (a) Picture of the WDM RX beamforming setup indicating the EPSoC, optic fiber bundle, and transmitting piezo attached to a goniometer that sets the transmission angle. (b) Beam profiles acquired from post-processed time-domain MRR responses.

power from the laser diode as well as resonance mismatch. The experimental setup, with a piezo mounted on a goniometer to insonify the EPSoC at a variable angle is shown in Fig. 14(a). Using the tuning controller locking algorithm described above, 8 PD-MRRs are locked onto the optimal slope bias point of separate optical modes of the input comb. Next, the chip is insonified and the digitized responses are serialized and transmitted to an FPGA for post-processing.

To acquire a beam profile, the de-serialized MRR outputs are bandpass filtered and summed while sweeping the delay settings. The ADC sample rate of 50MHz translates to a delay resolution of 20ns, which for a 5MHz ultrasonic pulse corresponds to a steering resolution of:

$$\theta_{res} = \sin^{-1} \frac{\tau_{res}c}{d} \simeq 7.5^{\circ},$$
 (13)

where  $\tau_{res}$  is the delay resolution, c=1500 m/s the speed of sound in water, and  $d=220 \mu \text{m}$  the sensor pitch of the array.

The steering resolution is validated by obtaining three beam profiles with the goniometer adjusted to transmit at  $0^{\circ}$ ,  $7.5^{\circ}$ , and  $15^{\circ}$ . The corresponding beam profiles are plotted in Fig. 14(b). To improve the delay resolution, the time-domain BPF responses are also interpolated before the delay-and-sum is applied. It can be seen that the peaks of the beam profiles correspond well with the transmitter angle, while the lateral resolution (FWHM<sub>beam</sub>) is in close agreement to the theoretical expectation. This experiment constitutes the first

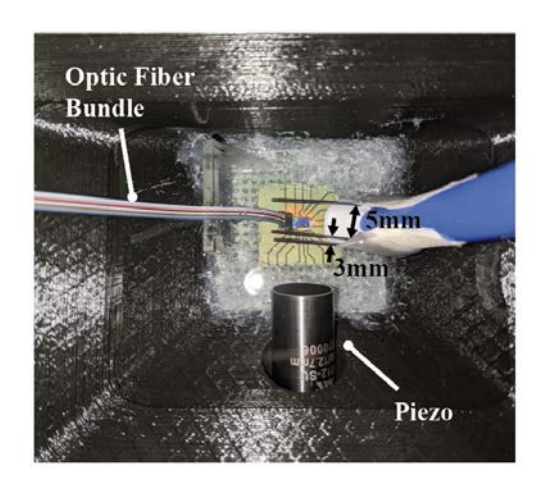
demonstration of a real-time, multi-channel WDM optical ultrasound receiver [25].

# F. Three-Needle Reflection Experiment

Lastly, a reflection imaging experiment was performed. Three needles, spaced 3 – 5mm to one another and taped to a rod that was suspended over the EPSoC, constituted a commonly used ultrasound imaging phantom. Ultrasound excitation was provided by a commercial piezo (Mana E5012-SU, 12.7mm, flat, 5MHz center frequency) screwed to the side of a modified water tank, as shown in Fig. 15(a).

A PD-MRR with the heater turned fully ON to enhance the responsivity was interrogated by a CW laser parked on the blue side of the Lorentzian. The bandpass filtered time-domain received waveform as well as the experimental setup are shown in Fig. 15(b). The difference in the time-of-arrival between the received reflections is consistent with the needle spacing and the speed of ultrasound in water (c=1500m/s), and serves as a sanity check for this experiment. Note, that the piezo transducer used in this experiment is screwed on the tank in an upward angle of  $\approx 15^{\circ}$ . This means that the total ToF is expected to correspond to double the spacing between the needles (6mm and 10mm respectively).

No B-mode imaging results were included in this experiment since the position of the TX on one side of the tank (Fig. 15) would lead to an image with additional reflections



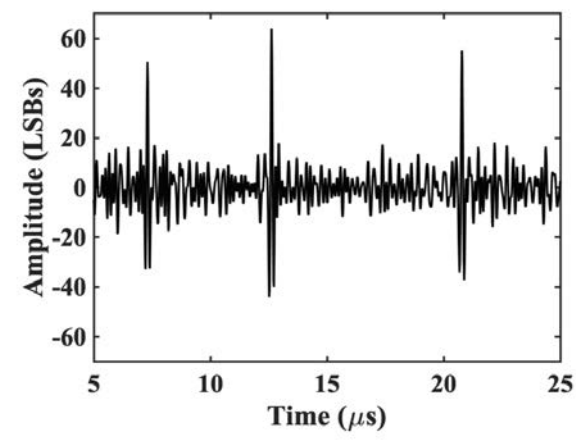


Fig. 15. (a) 3 needle-reflection experimental setup, (b) Single PD-MRR filtered (BPF: 2.5-7.5MHz) time-domain responses.

TABLE III COMPARISON WITH THE STATE OF THE ART – UPDATED

Reference	Nature '21 [52]	JSSC '17 [6]	JSSC '17 [8]	ISSCC '21 [14]	ISSCC '22 [53]	This Work
Process [nm]	200mm IMEC	28 SOI	180	130 BCD	180 BCD	45 SOI
Transducer	MRR	CMUT	PZT	CMUT	PZT	MRR
Transducer Size [μm]	20	250	150	208	100	10
Transducer Center Frequency [MHz]	26	5	5	5	10	5
Transducer BW [MHz]	27	10	5	9	8	>30
Transducer Sensitivity [mV/kPa or fm/kPa]	35k	2	-	-	-	40
Integration Method	Passive	Flip-Chip	3-D Direct	3-D Bond	3-D Direct	Monolithic *
Delay Resolution [ns]	NA	8.33	NA	6.25	12.5	20
NEP [kPa]	0.005	0.12	-	-	-	0.996
NEP density [Pa/ $\sqrt{\text{Hz}}$ ]	0.0013	0.037	-	-	-	0.48
SNDR [dB]	NA	58.9 <sup>†</sup>	51 <sup>‡</sup>	54.1	54 <sup>‡</sup>	25.5 <sup>††</sup>
Channel Reduction	Single Sensor	16	9	8	4	8
Power / Sense el. [mW]	NA (off-chip	17.5	0.27	0.66	1.17	0.43
Power / Rx el. [mW]	detection)					7.88
Area / Sense el. [mm <sup>2</sup> ]	NA (off-chip	0.041	0.0225	0.0225 0.043	0.04	0.01
Area / Rx el. [mm <sup>2</sup> ]	detection)		0.0223			0.042

 $<sup>^\</sup>dagger$  Peak, measured at 64-ch beamformer output,  $^\ddagger$  Peak,  $^{\dagger\dagger}$  Measured at -6.7dBFS.

from the opposite side of the tank. Combining the reflection and beam steering experiments we should in principle be able to provide B-mode images with an improved setup.

#### V. DISCUSSION AND FUTURE DIRECTIONS

Table III compares our work with the state of the art. Our EPSoC achieves record high power efficiency and area density, while being the first optical ultrasound receiver implementation that offers an 8 channel reduction through real-time WDM. It also constitutes a unique single chip solution in a commercially available CMOS-SOI process, requiring no 3-D integration of the transducer on top of the ASIC. On the downside, the SNDR and NEP values do not compare favorably to the state-of-the-art.

Lowering the total noise is the main knob to improve both the SNDR and NEP. The increased sensor density of our EPSoC can help to that end. Seeing as the noise sources are uncorrelated, the SNDR will be increased  $\propto \sqrt{N}$ , where N is the total number of sensors used to form an ultrasonic image. Thus, an array comprised of 1000 sensors, can get 15dB SNDR benefit, making for >40dB instantaneous SNDR, even

at the highest gain setting. Combined with the gain tunability and operation mode switching offered by the  $R_f$  and  $I_{DAC}$ s respectively, the goal of >70dB SNDR set in Section III-A can be met. Additionally, redesigning the ADC to increase its FS range, which was not optimized for this application due to limited design time, can significantly increase the instantaneous electronic dynamic range. However, as mentioned above, the overall DR was limited by the ring linear operating range, and was expected to suffice for this application. Given that this prototype was meant to serve as a proof of the remote optical ultrasound concept no significant effort was put in optimizing the ADC.

Increasing detector sensitivity can also boost the achieved NEP. MRRs with  $10 \times$  higher Q-factors will be employed in the next EPSoC generation and can proportionately increase sensitivity as can be seen by Eqs (1), (3). Devices of Q-factors up to 200k have been measured in this platform [29]. At the same time, using phase detection schemes has been show to offer a 30% improvement in sensitivity [54], and can be incorporated in our architecture with minimal area overhead. Finally, partial etching of the buried oxide (BOX) of the silicon

<sup>\*</sup>The term "monolithic" refers to the integration of the sensors and the receiver circuitry on a single chip.

die exposes the optical mode more, amplifying the effect of the waveguide thickness deformation on the refractive index and consequently the resonant shift. A 100nm partial BOX etch can improve  $S_{int}$  by  $7\times$  as shown in [55].

In summary, combining high-Q MRRs in a coherent sensing scheme, with sensor chips having partially etched BOX can boost sensitivity by up to almost 2 orders of magnitude (up to 1.3\*10\*7), with zero overhead in die area and system complexity of the sensor chip and minimal overhead on the receiver chip. Such an implementation will be on par with current state-of-the-art MRR based approaches [20] in terms of sensitivity with a projected NEP = 11Pa.

Another natural concern is the competitiveness of a full transceiver system based on MRR receivers, compared to a PZT matrix implementation with the same aperture which will have both TX and RX functionality. However, the increased area and power efficiency as well as the superior sensitivity offered by the electronic-photonic receivers is sufficient to counterbalance both the loss of aperture and TX beamforming gains.

For example, a system occupied primarily by MRR RX sensors with a smaller piezoelectric TX array in an adjacent companion chip that would occupy 10% of the total aperture, would be a competitive alternative. The proposed area distribution would lead to a 10× reduction in transmit gain, compared to a piezo-electric based implementation with the same aperture. However, MRR sensors can be arrayed in a 50μm pitch, while the lowest reported pitch to date for piezoelectric endoscopic arrays is 100 µm [56]. The area efficiency benefit is also apparent from our initial prototype which has an effective sensing area of 0.01mm<sup>2</sup>. The higher area efficiency leads to an increase of  $4\times$  in the overall RX gain, compared to the PZT matrix counterparts. Additionally, such a transceiver can be combined with the high sensitivity MRRs mentioned above which, surpass by almost 2 orders of magnitude the state-of-the-art piezoelectric elements of the same size [57] in terms of achieved NEP.

Thus, factoring in the superiority in area efficiency and sensitivity of the innovative optical RX, the proposed system could surpass the performance of state-of-the-art PZT matrix based full transceiver systems, at the expense of the increased complexity of co-packaging the companion chip. Such a system would also retain the benefit of reduced cable count, ultra-low power, increased resolution and superior sensor BW, compared to a PZT transceiver.

Of course, this prototype is the first step towards an alloptical approach, where the transmit ultrasound will be photoacoustically excited. Improved efficiency photoacoustic generation has been demonstrated in the past decade using materials with strong optical absorption, high thermal conductivity, and low optical reflectivity, while simultaneously designing the film thickness to equal the optical absorption length [58]–[60]. Integrating the PDMS thin film in [58] in a  $250 \times 250 \mu m^2$  aperture, 12 MPa ultrasound pulses can be generated while dissipating only 2.3 mW.

Also interesting in an all optical approach, is the multimodal imaging potential. This can be achieved through the use of a dichroic filter that absorbs in a certain wavelength and is transparent at another one [27]. Using two separate pulsed laser sources can enable switching between conventional ultrasound and photoacoustic imaging mode. Combining the structural details captured by conventional ultrasound with the finer features captured by the high optical absorption contrast in photoacoustics will render high-quality 3-D volumetric images. Consequently, MRR-based receiver arrays, cointegrated with efficient PA ultrasound generation structures in implementations beyond our first EPSoC prototype will be great candidates for next-generation all-optical multi-modal ultrasound imaging probes.

## VI. CONCLUSION

We have presented a first-of-its-kind EPSoC that has the with an MRR-based sensor in its core, and co-integrated active resonance tuning and signal conditioning circuitry in a compact dual-chip solution. This dual-chip architecture takes advantage of the photonic nature of this sensor which, combined with the on-chip thermal resonance control, enables the replacement micro-coax cables with optic fibers thus significantly increasing I/O density, to remote the power and area-hungry AFE outside the probe tip. Leveraging the above architectural aspects this prototype has also demonstrated the first true optical WDM ultrasound receiver array with zero area and power overhead. Such an architecture can be particularly beneficial for endoscopic applications, which require real-time volumetric imaging, using dense, low-power two-dimensional sensor arrays, and constitutes a competitive alternative to existing state-of-the-art technologies using PMUT and CMUT transducers.

# ACKNOWLEDGMENT

We thank the NSF, Berkeley Wireless Research Center and Santec for support and Ayar Labs for providing the EPSoC manufacturing.

## REFERENCES

- S.-J. Hong, B.-K. Kim et al., "Effect of intravascular ultrasound–guided vs angiography-guided everolimus-eluting stent implantation: the ivusxpl randomized clinical trial," *Jama*, vol. 314, no. 20, pp. 2155–2163, 2015.
- [2] K. Otani, M. Takeuchi et al., "Assessment of the aortic root using realtime 3d transesophageal echocardiography," Circulation Journal, vol. 74, no. 12, pp. 2649–2657, 2010.
- [3] I. S. Salgo, "Three-dimensional echocardiographic technology," Cardiology clinics, vol. 25, no. 2, pp. 231–239, 2007.
- [4] T. V. Scohy, G. Matte et al., "A new transesophageal probe for newborns," *Ultrasound in medicine & biology*, vol. 35, no. 10, pp. 1686– 1689, 2009.
- [5] E. Brunner, "Ultrasound system considerations and their impact on frontend components," *Analog Devices*, vol. 36, pp. 1–19, 2002.
- [6] M.-C. Chen, A. P. Perez et al., "A pixel pitch-matched ultrasound receiver for 3-d photoacoustic imaging with integrated delta-sigma beamformer in 28-nm utbb fd-soi," *IEEE journal of solid-state circuits*, vol. 52, no. 11, pp. 2843–2856, 2017.
- [7] J. Li, Z. Chen et al., "A 1.54 mw/element 150μm-pitch-matched receiver asic with element-level sar/shared-single-slope hybrid adcs for miniature 3d ultrasound probes," in 2019 Symposium on VLSI Circuits. IEEE, 2019, pp. C220–C221.
- [8] C. Chen, Z. Chen et al., "A front-end asic with receive sub-array beamforming integrated with a 32 × 32 pzt matrix transducer for 3-d transesophageal echocardiography," *IEEE Journal of Solid-State Circuits*, vol. 52, no. 4, pp. 994–1006, 2017.

- [9] U. S. Food and Drug Administration (FDA), "Marketing clearance of diagnostic ultrasound systems and transducers." [Online]. Available: https://www.fda.gov/media/71100/download
- [10] Q. Liu, C. Chen et al., "A mixed-signal multiplexing system for cablecount reduction in ultrasound probes," in 2015 IEEE International Ultrasonics Symposium (IUS). IEEE, 2015, pp. 1–4.
- [11] G. Jung, C. Tekes et al., "A reduced-wire ice catheter asic with tx beamforming and rx time-division multiplexing," *IEEE transactions on biomedical circuits and systems*, vol. 12, no. 6, pp. 1246–1255, 2018.
- [12] K. Latham, C. Samson et al., "A 30-mhz, 3-d imaging, forward-looking miniature endoscope based on a 128-element relaxor array," *IEEE Transactions on Ultrasonics, Ferroelectrics, and Frequency Control*, vol. 68, no. 4, pp. 1261–1271, 2020.
- [13] E. Kang, Q. Ding et al., "A reconfigurable ultrasound transceiver asic with 24×40 elements for 3-d carotid artery imaging," *IEEE Journal of Solid-State Circuits*, vol. 53, no. 7, pp. 2065–2075, 2018.
- [14] N. Sanchez, K. Chen et al., "34.1 an 8960-element ultrasound-on-chip for point-of-care ultrasound," in 2021 IEEE International Solid-State Circuits Conference (ISSCC), vol. 64. IEEE, 2021, pp. 480–482.
- [15] E. J. Alles, N. F. Sheung *et al.*, "A reconfigurable all-optical ultrasound transducer array for 3d endoscopic imaging," *Scientific reports*, vol. 7, no. 1, pp. 1–9, 2017.
- [16] E. Z. Zhang and P. C. Beard, "A miniature all-optical photoacoustic imaging probe," in *Photons plus ultrasound: imaging and sensing 2011*, vol. 7899. International Society for Optics and Photonics, 2011, p. 78991F.
- [17] G. Wissmeyer, D. Soliman *et al.*, "All-optical optoacoustic microscope based on wideband pulse interferometry," *Optics letters*, vol. 41, no. 9, pp. 1953–1956, 2016.
- [18] A. Rosenthal, D. Razansky, and V. Ntziachristos, "High-sensitivity compact ultrasonic detector based on a pi-phase-shifted fiber bragg grating," *Optics letters*, vol. 36, no. 10, pp. 1833–1835, 2011.
- [19] X. Zhu, Z. Huang et al., "Ultrasonic detection based on polarization-dependent optical reflection," Optics letters, vol. 42, no. 3, pp. 439–441, 2017.
- [20] S. Leinders, W. Westerveld et al., "A sensitive optical micro-machined ultrasound sensor (omus) based on a silicon photonic ring resonator on an acoustical membrane," Scientific reports, vol. 5, p. 14328, 2015.
- [21] L. V. Wang and S. Hu, "Photoacoustic tomography: in vivo imaging from organelles to organs," *science*, vol. 335, no. 6075, pp. 1458–1462, 2012.
- [22] W. J. Westerveld, M. Mahmud-Ul-Hasan et al., "Sensitive, small, broadband and scalable optomechanical ultrasound sensor in silicon photonics," *Nature Photonics*, vol. 15, no. 5, pp. 341–345, 2021.
- [23] C. Zhang, T. Ling et al., "Ultrabroad bandwidth and highly sensitive optical ultrasonic detector for photoacoustic imaging," Acs Photonics, vol. 1, no. 11, pp. 1093–1098, 2014.
- [24] W. J. Westerveld, M. Mahmud-Ul-Hasan et al., "Opto-mechanical ultrasound sensor based on sensitive silicon-photonic split rib-type waveguide," in 2019 Conference on Lasers and Electro-Optics Europe & European Quantum Electronics Conference (CLEO/Europe-EQEC). IEEE, 2019, pp. 1–1.
- [25] P. Zarkos, S. Buchbinder *et al.*, "Fully integrated electronic-photonic ultrasound receiver array for endoscopic imaging applications in a zerochange 45nm cmos-soi process," in 2021 Symposium on VLSI Circuits. IEEE, 2021, pp. 1–2.
- [26] C. Chen, S. B. Raghunathan et al., "A prototype pzt matrix transducer with low-power integrated receive asic for 3-d transesophageal echocardiography," *IEEE transactions on ultrasonics, ferroelectrics, and frequency control*, vol. 63, no. 1, pp. 47–59, 2015.
- [27] B.-Y. Hsieh, S.-L. Chen et al., "All-optical scanhead for ultrasound and photoacoustic imaging—imaging mode switching by dichroic filtering," *Photoacoustics*, vol. 2, no. 1, pp. 39–46, 2014.
- [28] P. Zarkos, O. Hsu, and V. Stojanović, "Ring resonator based ultrasound detection in a zero-change advanced cmos-soi process," in CLEO: QELS\_Fundamental Science. Optical Society of America, 2019, jW2A– 78.
- [29] J. S. Orcutt, B. Moss et al., "Open foundry platform for high-performance electronic-photonic integration," Optics express, vol. 20, no. 11, pp. 12222–12232, 2012.
- [30] C. Adamopoulos, P. Zarkos et al., "Lab-on-chip for everyone: Introducing an electronic-photonic platform for multiparametric biosensing using standard cmos processes," *IEEE Open Journal of the Solid-State Circuits Society*, 2021.
- [31] M. Wade, E. Anderson et al., "An error-free 1 tbps wdm optical i/o chiplet and multi-wavelength multi-port laser," in Optical Fiber

- Communication Conference. Optical Society of America, 2021, pp. F3C-6.
- [32] Y. Shi, S. Li *et al.*, "High channel count and high precision channel spacing multi-wavelength laser array for future pics," *Scientific reports*, vol. 4, no. 1, pp. 1–6, 2014.
- [33] T. J. Seok, V. Kopp et al., "High density optical packaging of high radix silicon photonic switches," in *Optical Fiber Communication Conference*. Optical Society of America, 2017, pp. Th5D–7.
- [34] V. I. Kopp, J. Park et al., "Chiral fibers: microformed optical waveguides for polarization control, sensing, coupling, amplification, and switching," *Journal of Lightwave Technology*, vol. 32, no. 4, pp. 605–613, 2013.
- [35] "Hitachi micro-coax cables datasheet," http://www.elimec.co.il/\_ Uploads/dbsAttachedFiles/HCA\_Med.pdf, accessed: 2021-08-02.
- [36] P. R. Hoskins, K. Martin, and A. Thrush, Diagnostic ultrasound: physics and equipment. CRC Press, 2019.
- [37] D. F. Lemmerhirt, A. Borna et al., "Cmut-in-cmos 2d arrays with advanced multiplexing and time-gain control," in 2014 IEEE International Ultrasonics Symposium. IEEE, 2014, pp. 582–586.
- [38] W. Bae, "Cmos inverter as analog circuit: An overview," Journal of Low Power Electronics and Applications, vol. 9, no. 3, p. 26, 2019.
- [39] S. M. Park and C. Toumazou, "A packaged low-noise high-speed regulated cascode transimpedance amplifier using a 0.6 μm n-well cmos technology," in *Proceedings of the 26th European Solid-State Circuits Conference*. IEEE, 2000, pp. 431–434.
- [40] C. Kromer, G. Sialm et al., "A low-power 20-ghz 52-db/spl omega/transimpedance amplifier in 80-nm cmos," *IEEE Journal of Solid-State Circuits*, vol. 39, no. 6, pp. 885–894, 2004.
- [41] B. Razavi, "A 622 mb/s 4.5 pa//spl radic/hz cmos transimpedance amplifier [for optical receiver front-end]," in 2000 IEEE International Solid-State Circuits Conference. Digest of Technical Papers (Cat. No. 00CH37056). IEEE, 2000, pp. 162–163.
- [42] C. Ciofi, F. Crupi et al., "A new circuit topology for the realization of very low-noise wide-bandwidth transimpedance amplifier," *IEEE Transactions on Instrumentation and Measurement*, vol. 56, no. 5, pp. 1626–1631, 2007.
- [43] "BAG github repo webpage," https://github.com/ucb-art/BAG\_framework, accessed: 2021-08-02.
- [44] J. Han, W. Bae et al., "Laygo: A template-and-grid-based layout generation engine for advanced cmos technologies," *IEEE Transactions* on Circuits and Systems I: Regular Papers, vol. 68, no. 3, pp. 1012– 1022, 2021.
- [45] C. Chen, Z. Chen et al., "A 0.91 mw/element pitch-matched frontend asic with integrated subarray beamforming adc for miniature 3d ultrasound probes," in 2018 IEEE International Solid-State Circuits Conference-(ISSCC). IEEE, 2018, pp. 186–188.
- [46] E. Timurdogan, C. M. Sorace-Agaskar et al., "An ultralow power athermal silicon modulator," *Nature communications*, vol. 5, no. 1, pp. 1–11, 2014.
- [47] C. Li, R. Bai et al., "Silicon photonic transceiver circuits with microring resonator bias-based wavelength stabilization in 65 nm cmos," *IEEE* journal of solid-state circuits, vol. 49, no. 6, pp. 1419–1436, 2014.
- [48] S. Moazeni, S. Lin et al., "A 40-gb/s pam-4 transmitter based on a ringresonator optical dac in 45-nm soi cmos," *IEEE Journal of Solid-State Circuits*, vol. 52, no. 12, pp. 3503–3516, 2017.
- [49] B. Peng, T. Barwicz et al., "A cmos compatible monolithic fiber attach solution with reliable performance and self-alignment," in *Optical Fiber Communication Conference*. Optical Society of America, 2020, pp. Th31–4.
- [50] P. Zarkos, S. Buchbinder et al., "Monolithically integrated electronic-photonic ultrasound receiver using microring resonator," in CLEO: QELS\_Fundamental Science. Optical Society of America, 2021, pp. STh1H–2.
- [51] C. Sun, M. Wade et al., "A 45 nm cmos-soi monolithic photonics platform with bit-statistics-based resonant microring thermal tuning," *IEEE Journal of Solid-State Circuits*, vol. 51, no. 4, pp. 893–907, 2016.
- [52] C. Zhang, S.-L. Chen et al., "Imprinted polymer microrings as high-performance ultrasound detectors in photoacoustic imaging," Journal of Lightwave Technology, vol. 33, no. 20, pp. 4318–4328, 2015.
- [53] P. Guo, F. Fool et al., "A 1.2 mw/channel 100μm-pitch-matched transceiver asic with boxcar-integration-based rx micro-beamformer for high-resolution 3d ultrasound imaging," in 2022 IEEE International Solid-State Circuits Conference (ISSCC), vol. 65. IEEE, 2022, pp. 496–498.
- [54] M. Terrel, M. J. Digonnet, and S. Fan, "Ring-coupled mach-zehnder interferometer optimized for sensing," *Applied optics*, vol. 48, no. 26, pp. 4874–4879, 2009.

- [55] C. Adamopoulos, A. Gharia et al., "Electronic-photonic platform for label-free biophotonic sensing in advanced zero-change cmos-soi process," in CLEO: QELS\_Fundamental Science. Optical Society of America, 2019, pp. JW2A–81.
- [56] P. Guo, Z.-Y. Chang et al., "A pitch-matched low-noise analog frontend with accurate continuous time-gain compensation for high-density ultrasound transducer arrays," *IEEE Journal of Solid-State Circuits*, 2022
- [57] A. M. Winkler, K. I. Maslov, and L. V. Wang, "Noise-equivalent sensitivity of photoacoustics," *Journal of biomedical optics*, vol. 18, no. 9, p. 097003, 2013.
- [58] B.-Y. Hsieh, J. Kim et al., "A laser ultrasound transducer using carbon nanofibers–polydimethylsiloxane composite thin film," Applied Physics Letters, vol. 106, no. 2, p. 021902, 2015.
- [59] E. Biagi, F. Margheri, and D. Menichelli, "Efficient laser-ultrasound generation by using heavily absorbing films as targets," *ieee transactions* on ultrasonics, ferroelectrics, and frequency control, vol. 48, no. 6, pp. 1669–1680, 2001.
- [60] H. W. Baac, J. G. Ok et al., "Carbon-nanotube optoacoustic lens for focused ultrasound generation and high-precision targeted therapy," *Scientific reports*, vol. 2, no. 1, pp. 1–8, 2012.



Panagiotis Zarkos (S'14, M'22) received the B.S. degree in electrical and computer engineering from National Technical University of Athens, Athens, Greece, in 2015, and the M.S. and PhD degrees in electrical engineering and computer sciences from the University of California at Berkeley, Berkeley, CA, USA, in 2019 and 2021 respectively.

He held an internship position at the PHY Research Laboratory, Intel Corporation, Hillsboro, OR, USA, where he worked on energy-efficient, high-speed transceiver architectures based on silicon pho-

tonics. His current research interests include analog and mixed-signal IC design and the design and modeling of electronic-photonic integrated systems for biomedical sensors, focusing on endoscopic ultrasound receivers.



**Sidney Buchbinder** received the B.S. degree in electrical engineering from the California Institute of Technology (Caltech), Pasadena, CA, USA, in 2015. He is currently pursuing the Ph.D. degree at the University of California at Berkeley, Berkeley, CA, USA.

His research interests include photonic design automation and verification, and the design of analog electronic-photonic integrated systems. He has held an internship position at Ayar Labs, where he worked on integrated photonic system design.



Christos Adamopoulos (M'21) received the B.S. degree in electrical and computer engineering from National Technical University of Athens, Athens, Greece, in 2015, and the M.S. and PhD degrees in electrical engineering and computer sciences from the University of California at Berkeley, Berkeley, CA, USA, in 2019 and 2021 respectively.

He has held internship positions at Infineon Technologies, Munich, Germany and Apple, Cupertino, CA, USA. His current research interests include analog and mixed-signal integrated circuits and the

design and implementation of electronic-photonic integrated systems for biosensing lab-on-chip applications.



Sarika Madhvapathy received the B.S. degree in 2020 and the M.S. degree in 2021 from the University of California at Berkeley, Berkeley, CA, USA. She is now pursuing a Ph.D. degree at the University of California at Berkeley, Berkeley, CA, USA.

She held two internship positions at Apple, Cupertino, CA, USA, where she worked on system-on-chip power grid integrity analysis. Her research interests include electronic-photonic integrated systems and analog integrated circuits.



Olivia Hsu Olivia Hsu received the B.S. degree in electrical engineering and computer science from the University of California at Berkeley, Berkeley, CA, USA in 2019. She is currently pursuing the Ph.D. degree at Stanford University, Stanford, CA, USA

Olivia held internships at Apple Inc., Cupertino, CA, USA doing CPU design verification. She has also held an internship position at Ayar Labs, Santa Clara, CA, USA, where she worked on digital design, physical design, and design verification. Her

current research interests include domain-specific accelerators, languages, and architectures with a focus on compiling sparse applications to reconfigurable hardware architectures.



**Jake Whinnery** is working towards his B.S. degree in mechanical engineering from the University of California at Berkeley, Berkeley, CA, USA.

Jake held an internship position at Tesla in Palo Alto, CA, USA, doing mechanical design and product development work for the autopilot team. Prior to that, he held an internship position on the propulsion team at Relativity Space in Long Beach, CA, USA, doing gimbal, thrust vector hardware, and exhaust duct design and analysis. Additional roles include process engineering intern at the upstream

technologies division of Procter and Gamble (P&G) in Cincinnati, Ohio, USA, microfluidics design and product development intern at Triple Ring Technologies in Newark, CA, USA, and mechanical design and testing intern for the capture and analysis of microorganisms in fog clouds for the National Aeronautics and Space Administration (NASA), Moffett Field, CA, USA.



Pavan Bhargava (S'14) received the B.S. degree in electrical engineering from the University of Maryland at College Park, College Park, MD, USA,in 2014. He is currently pursuing the Ph.D. degree in electrical engineering from the University of California at Berkeley, Berkeley, CA, USA. He held internships at the U.S. Army Research Laboratory, Adephi, MD, USA, where he developed low-power biosensors. He is with the AyarLabs, Emeryville, CA, USA, where he focuses on high-speed analog/mixed signal design for optical receivers. His

current research interests include modeling and designing fully integrated optical beam-steering systems for solid-state LiDAR applications.



Vladimir Stojanović (Senior Member, IEEE) received the Dipl.Ing. degree from the University of Belgrade, Belgrade, Serbia, in 1998, and the Ph.D. degree in electrical engineering from Stanford University, Stanford, CA, USA, in 2005. He was with Rambus, Inc., Los Altos, CA, USA, from 2001 to 2004, and the Massachusetts Institute of Technology, Cambridge, MA, USA, as an Associate Professor, from 2005 to 2013. He is currently a Professor of electrical engineering and computer sciences with the University of California at Berkeley, Berkeley,

CA, USA and a faculty co-director of the Berkeley Wireless Research Center (BWRC). His current research interests include design, modeling, and optimization of integrated systems, from CMOS-based VLSI blocks and interfaces to system design with emerging devices such as NEM relays and silicon photonics, design and implementation of energy-efficient electrical and optical networks, and digital communication techniques in high-speed interfaces and high-speed mixed-signal IC design. Dr. Stojanović was a recipient of the 2006 IBM Faculty Partnership Award, the 2009 NSF CAREER Award, and the 2008 ICCAD William J. McCalla, the 2008 IEEE TRANSACTIONS ON ADVANCED PACKAGING and the 2010 ISSCC Jack Raper Best Paper and 2020 ISSCC Best Forum Presenter Awards. He was an IEEE Solid-State Circuits Society Distinguished Lecturer from 2012 to 2013.